Thermodynamic properties of paramagnetic α- and β-Mn from first principles: The effect of transverse spin fluctuations

Hossein Ehteshami[1,*] and Pavel A. Korzhavyi[1,2]

[1]*Department of Materials Science and Engineering, KTH Royal Institute of Technology, SE-10044, Stockholm, Sweden*

[2]*Materials Modeling and Development Laboratory, National University of Science and Technology "MISIS," 119049 Moscow, Russia*

(Received 16 October 2017; revised manuscript received 6 December 2017; published 29 December 2017)

First-principles-based thermodynamic modeling of cubic α and β phases of Mn represent a challenge due to their structural complexity and the necessity of simultaneous treatment of several types of disorder (electronic, magnetic, and vibrational) that have very different characteristic time scales. Here we employ mean-field theoretical models to describe the different types of disorder and then we connect each layer of theory to the others using the adiabatic principle of separating faster and slower degrees of freedom. The slowest (vibrational) degrees of freedom are treated using the Moruzzi, Janak, and Schwarz formalism [Phys. Rev. B **37**, 790 (1988)] of the Debye-Grüneisen model parametrized based on the first-principles calculated equation of state which includes the free-energy contributions due to the fast (electronic and magnetic) degrees of freedom via the Fermi-Dirac distribution function and a mean-field theory of transverse spin fluctuations. The magnetic contribution due to transverse spin fluctuations has been computed self-consistently within the disordered local moment picture of the paramagnetic state. The obtained results for thermodynamic properties such as lattice parameter, linear thermal expansion coefficient, and heat capacity of both phases show a good agreement with available experimental data. We also tested the assumption about the nature (localized versus delocalized) of magnetic moment on site IV in α-Mn and site I in β-Mn on the thermodynamic properties of these two phases. Similar to the findings of experimental studies, we conclude that magnetic moment on site IV in α-Mn is not of a localized character. However, a similar analysis suggests that the magnetic moment of site I in β-Mn should be treated as localized.

DOI: 10.1103/PhysRevMaterials.1.073803

I. INTRODUCTION

Because of its practical and theoretical importance, elemental manganese has been the subject of many studies. The first of four allotropic forms of manganese, α-Mn is stable from 0 to 1000 K and is believed to be the most complex of all elements considering its magnetic and atomic structure. Below the Néel temperature of 97 K, α-Mn forms a long-range antiferromagnetic (AFM) order. In the paramagnetic state ranging from 100 to 1000 K, α-Mn has a complex cubic structure with 58 atoms per body-centered unit cell with four inequivalent sites. As will be discussed thoroughly in Sec. II A, neutron diffraction data [1–4] suggest a noncollinear antiferromagnetic structure below 97 K. Below the Néel temperature, a tetragonal distortion appears and the symmetry of crystal structure becomes lower due to magnetoelastic effect [4]. The distorted tetragonal unit cell still contains 58 Mn atoms, but instead of four there are six magnetically inequivalent sites though the number of crystallographically inequivalent sites remains the same. It is worth mentioning that magnetoelastic effect has been observed in other elements and compounds [5]. For example, it occurs upon quenching of γ-Mn, a high-temperature face-centered-cubic phase, that also undergoes an antiferromagnetic ordering.

Manganese is in the middle of the 3*d* transition metal series and has a half-filled electron shell. One might expect that such an electronic configuration causes various crystal structure instabilities. However, experimentally we know that α-Mn phase is stable in a wide temperature range. One reason for the structural stability of α-Mn could be that Mn atoms with different magnetic moments in the unit cell behave like atoms having different sizes [6]. In this way, a *self-intermetallic* compound is formed where elemental Mn actually forms an intermetallic compound of Mn atoms with different electronic configurations [7]. Using Laguerre tessellation and by constructing different atomic environments for inequivalent Mn sites, as will be discussed in Sec. III, we effectively take into account the fact that the electronic structure of Mn atoms occupying one inequivalent site should be different from that of Mn at another inequivalent site of the same crystal structure.

At temperatures above 1000 K, α-Mn transforms into another phase of Mn called β-Mn. This phase is a complex cubic crystal structure, with 20 atoms per cell. The β phase can also be quenched down to very low temperatures. The magnetic properties of β-Mn at low temperatures seem to be quite unusual. As we discuss in the Sec. II B, there is evidence for large spin fluctuations on site II at very low temperatures and that site I is probably nonmagnetic. We will then address the effect of nonzero magnetic moment at site I on thermodynamic properties of the β phase. Theoretically and experimentally, it has been confirmed that no magnetic order appears in β-Mn down to 1.4 K. Several authors conjectured that this behavior is a result of the geometric frustration of Mn on the site II which forms a three-dimensional triangular lattice.

There are a number of theoretical studies addressing the structural and magnetic properties of α- and β-Mn [6,8–12]. Nevertheless, the thermodynamic properties of paramagnetic α- and β-Mn have not been subject to extensive research. In both cases, we are dealing with a paramagnetic state at elevated temperatures. Treating paramagnetic disorder in

*heht@kth.se

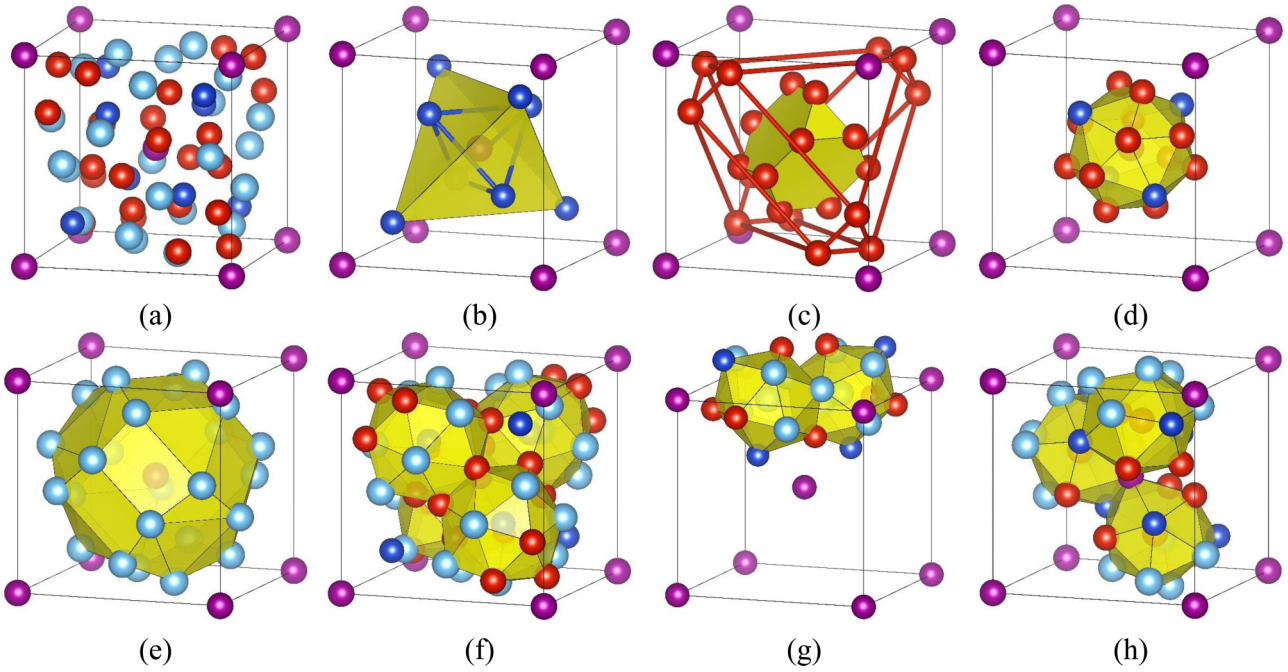

FIG. 1. Analysis of crystal structure of α-Mn. (a) Cubic representation of α-Mn. MnI atoms, located at center and corners of the cell, denoted by purple color and MnII, MnIII, and MnIV atoms by dark blue, light blue, and red colors, respectively. (b) Tetrahedra around MnI composed of MnII atoms (For details please see the text). (c) Solid color is Friauf polyhedron made of MnIV atoms around MnI. Wireframe structure is a truncated tetrahedron of MnIV atoms. (d) First NN shell around MnI. (e) Second NN shell around MnI made of MnIII atoms. Coordination shells around (f) MnII, (g) MnIII, and (h) MnIV.

complex structures such as α- and β-Mn is a formidable task due to the rather large number of atoms in the respective unit cells. One has to also include other types of thermal disorder (electronic, vibrational) in the first-principles-based simulations in order to compute the thermodynamic properties.

The bridge between the macroscopic properties and microscopic properties is the partition function. To calculate the Helmholtz free energy, the partition function must be sampled with respect to possible degrees of freedom. It is a highly multidimensional phase-space that must be sampled in the case of complex structures. Considering the purpose of such a task, which includes obtaining statistically averaged quantities in the thermodynamic limit, direct sampling such phase-spaces with the accuracy required for thermodynamic modeling is not feasible, so one must find alternative approaches. In such cases, suitable approximations and models can be quite useful. Following this line of reasoning, in this work we employ adiabatic approximation to study thermodynamic properties of α- and β-Mn at elevated temperatures. Similar approach has been employed to study finite temperature properties of high-entropy alloys [13,14].

In particular, we address the problem of computing the thermodynamic properties of α- and β-Mn from first-principles based models of the Helmholtz free energy. A partitioning approach [15] was employed to calculate the free energy. In this scheme, different contributions (vibrational, magnetic and electronic) are separated following the rationale of adiabatic approximation and using a suitable mean field theory each contribution is calculated. Once the free energy is known, thermodynamic properties such as the thermal expansion coefficient and the heat capacity of two paramagnetic phases of Mn in their respective temperature ranges of thermodynamic stability will be calculated.

The present paper is organized as follows. In Sec. II the crystalline and magnetic structure of α- and β-Mn will be briefly reviewed. Section III describes our modeling approach to these systems. In Sec. IV, the results of calculations are be presented and analyzed.

II. MAGNETIC AND CRYSTAL STRUCTURE

A. α-Mn

The crystal structure of α-Mn is body-centred cubic (BCC), space group $T_d^3 - I4\bar{3}m$, with 29 atoms in the primitive cell (58 atoms per unit cell). These 58 Mn atoms occupy four crystallographic inequivalent sites. Type I sites (MnI) are located at the center and every corner of the unit cell (2 sites per cell). Eight type II atoms form two differently sized tetrahedra around site I; see Fig. 1(b). An edge of the smaller tetrahedron measures to $0.518a$, where a is the lattice parameter of the cubic unit cell, and an edge of the bigger tetrahedron equals to $0.897a$. The nearest-neighbor (NN) shell of site I consists of 12 atoms of type IV forming a polyhedron that is shown in yellow color in Fig. 1(c). The remaining 12 MnIV atoms form a truncated tetrahedron around the central MnI site; an edge of the truncated tetrahedron is $0.8896a$, shown as red wire-frame object in Fig. 1(c). The angle between the edges of the bigger and the smaller MnIV truncated tetrahedra is 90° and they are intertwined. The complete coordination shell of a MnI atom consists of the first neighbor shell of 12 MnIV atoms and the second neighbor shell of 4 MnII atoms that together form a Friauf polyhedron with the coordination number (CN) 16;

TABLE I. Crystallographic information and magnetic moments on inequivalent sites in α-Mn.

	MnI	MnII	MnIII	MnIV
Number of atoms	2	8	24 (8+16)	24 (8+16)
Coordination Number(CN)	16	16	13	12
Atomic radii ratio	1.21	1.11	1.10	1.00
Volume ratio	1.75	1.42	1.31	1.00
NN distance	0.309a	0.289a	0.263a	0.252a
Type of NN	MnIV	MnIII	MnIV	MnIV
Magnetic moment (μ_B)—Experiments				
Ref. [2], CL-AFM[a]	2.50(1.54)[b]	2.50(1.54)[b]	1.70(3.08)[b]	0.0(0.0)[b]
Ref. [3], CL-AFM	1.4	1.02	0.82	0.10
Ref. [4], CL-AFM	1.36	1.32	0.99	0.22
Ref. [4], NCL-AFM[c]	1.90	1.78	0.50(0.55)[d]	0.25(0.38)[d]
Ref. [7], NCL-AFM	2.83	1.83	0.76(0.48)[d]	0.60(0.66)[d]
Magnetic moment (μ_B)—Calculations				
Ref. [9], LMTO, CL-AFM	2.67	2.29	−0.59	0.52
Ref. [6], PAW, NCL-AFM	2.79	−2.22	1.00(−1.00)[d]	0
Ref. [6], LMTO, NCL-AFM	3.26	−2.69	1.11(−1.10)[d]	−0.06(0.07)[d]
Ref. [10], ASW, CL-AFM	1.79	±1.43	−0.40	−0.17
This work, EMTO, DLM	2.13(2.15)[e]	1.42(1.44)[e]	0.59(0.61)[e]	0.00(0.27)[e]

[a]Collinear (CL) model of antiferromagnetic (AFM) state.
[b]According to two different models for magnetic form factor, cf. Sec. II A.
[c]Noncollinear (NCL) model of AFM state.
[d]In NCL-AFM state, MnIII and MnIV split into two inequivalent sites.
[e]Averaged value assuming the magnetic moment on MnIV is quenched (allowed).

see Fig. 1(d). The next NN shell around MnI consists of 24 MnIII atoms and has a truncated cube shape with an edge of 0.717a; it may also be viewed as eight equilateral triangles and their connections; see Fig. 1(e). The coordination polyhedron around MnII is also a Friauf polyhedron with CN=16, composed of 1 MnI, 6 MnIII, and 9 MnIV type atoms; see Fig. 1(f). The coordination polyhedron around MnIII is composed of 6 MnIII, 5 MnIV, and 2 MnII atoms (CN=13); see Fig. 1(g). The coordination polyhedron around MnIV is an icosahedron (CN=12) composed of 1 MnI, 3 MnII, 5 MnIII, and 3 MnIV, as can be seen in Fig. 1(h). Experimentally, the low- and high-temperature crystal structures of α-Mn have been studied extensively [2,7,16]. There is a consensus among different experiments about the x, y, z parameters of the different atomic positions in the structure. We have adopted the structural parameters reported Ref. [16]. All the lengths reported above correspond to that set of values for internal coordinates.

The low-temperature magnetic structure of α-Mn has been the subject of debate. It is now accepted that α-Mn has a noncollinear antiferromagnetic structure below the Néel temperature T_N of 97 K. In spite of the unanimous agreement on the crystal and magnetic structure of the antiferromagnetic α-Mn phase, there are still ambiguities regarding the values of magnetic moments to be assigned to every site. The difficulty arises from the fact that different form factors lead to different magnetic moments. Shull and Wilkinson [1] were the first to study the antiferromagnetic structure of low-temperature α-Mn. For the high-temperature paramagnetic phase, they suggested that straightforward interpretation of the cross section data of neutron diffraction would lead to an average moment of 0.5 μ_B for each atom. However, they argued that a more realistic interpretation of results is to consider magnetic moments of 1.0 μ_B for 40% of atoms and and no moments for the remaining 60%.

In another neutron diffraction study, Kasper and Roberts [2] showed that each crystallographically inequivalent site has a different magnetic moment. Using two collinear magnetic models, they obtained two sets of magnetic moments that are shown in Table I. Using neutron diffraction method, Oberteuffer *et al.* [3] obtained magnetic moments for several temperatures that are also listed in Table I, assuming a collinear magnetic structure. The results of Kasper and Roberts and those of Oberteuffer *et al.* agree on the magnitude of moments. Using single crystals of α-Mn grown by the distillation method, Kunitomi *et al.* [4] studied the structural and magnetic properties of α-Mn by means of neutron diffraction. Based on collinear and noncollinear models, several sets of magnetic moments for different sites have been reported. A general trend for magnetic moments of different sites, $|\mu_I| > |\mu_{II}| > |\mu_{III}| > |\mu_{IV}|$, obtained in previous neutron diffraction studies, was also confirmed in their study. Comparing the various form factors, they concluded that a better agreement can be obtained if one assumes a noncollinear magnetic structure.

A different characterization method could shed more light on the magnetic structure. X-ray photo-emission spectra (XPS) measurement of paramagnetic α-Mn by McFreely *et al.* [18] provided new perspective about the nature of magnetic structure of the high-temperature α-Mn. Their results show that a localized moment of 2.5 μ_B exist on each site. It was noted in their study that this large magnetic moment, which contradicts the results of neutron scattering measurements, could be related to the correlation time that each of the two techniques can capture. XPS measurements can capture correlation time of 10^{-15} and longer, while neutron diffraction measurements can detect correlation time of 10^{-12}. So, the smaller moments

on sites MnIII and MnIV can be related to faster fluctuations on these two sites. The magnetic susceptibility measurements of Nagasawa and Uchinami [19] yielded an effective moment of 2.5 μ_B, which is comparable to that obtained by McFreely *et al.* [18].

Sliwko *et al.* [10] employed the augmented-spherical-wave (ASW) method to study α- and β-Mn based on the local-spin-density approximation (LSDA) for the exchange and correlation functional. For α-Mn, they assumed a collinear antiferromagnetic structure. In their model, the moments of two MnI sites are assumed to be antiparallel to each other. The four MnII atoms around a MnI site are assumed to form an antiferromagnetic configuration (two up and two down), while the 12 MnIV neighbors of each MnI site are assumed to be all coupled parallel to each other and antiparallel to the central MnI site. An objection has been raised by Hobbs *et al.* [6] that such a magnetic structure contradicts the experimental results of Kunitomi *et al.* [4] as well as the group theoretical analysis of the magnetic structure [20]. In their study, Sliwko *et al.* used the experimental lattice parameter in the calculations of magnetic structure and properties. It has been pointed out that there is a direct correlation between the nearest-neighbor distance (and coordination number) of an atom and its magnetic moment, which can also be seen from Table I. MnI has the longest NN distance, the highest coordination number, and the largest magnetic moment, while MnIV has the smallest NN distance, the lowest coordination number, and a vanishing magnetic moment.

The linear muffin-tin orbital (LMTO) method combined with the generalized gradient approximation (GGA) for the exchange-correlation functional has been used by Asada [9] to study the antiferromagnetic and paramagnetic states of α- and β-Mn. Asada calculated the equilibrium volume by minimizing the total energy with respect to lattice parameter. A collinear magnetic structure was assumed in the calculations. He reported that a magnetic structure in which the magnetic moment on MnIII is coupled antiparallel to the other three sites had a lower total energy than the paramagnetic state. As pointed out by Hobbs *et al.* [6], this magnetic structure is in clear contrast to experimental results. Since the equilibrium volume is overestimated in the study by Asada, the reported values of magnetic moments for the theoretical equilibrium volume are rather high. However, using experimental volume, lower values were reported for magnetic moments and they were closer to experimental data.

Hobbs *et al.* [6] comprehensively studied the noncollinear and collinear antiferromagnetic structures of α-Mn using the LMTO and the projector augmented wave (PAW) methods. They showed that the triangular network of MnIV atoms in the α-Mn causes a magnetic frustration and drives the system to develop a non-collinear magnetic structure. The results of Ref. [6] concerning the crystal and magnetic structure agree well with experimental data. In that study, it was further suggested that MnIII and MnIV could even be divided into three rather than two subgroups, causing the magnetic structure to have a lower symmetry than assumed before. Such lowering of magnetic symmetry may cause stronger deviation from the cubic symmetry, as discussed in Ref. [6]. However, it has been argued that the experimentally reported tetragonality of the low-temperature structure is small ($c/a = 0.99955$), so that the theoretically obtained additional lowering of the symmetry is on the border of accuracy of the calculations and a firm conclusion cannot be drawn.

B. β-Mn

Crystallographically, β-Mn is a complex simple cubic A13-type structure with 20 atoms in the unit cell, space group $P4_132$, with two inequivalent Mn sites: MnI in the 8(c) Wyckoff positions and MnII in the 12(d) positions. Like α-Mn, most substances with this symmetry are compounds or alloys. The coordination polyhedron around MnI is a distorted icosahedron consisting of 3 MnI and 9 MnII atoms that can be seen in Fig. 2(b). There are four type of distances in the first NN shell around MnI; a MnI-MnI distance of 0.374a (a is the lattice parameter of the cubic phase) and three MnI-MnII distances, 0.408a, 0.417a and 0.424a. MnII is coordinated by 14 atoms which form a Friauf polyhedron consisting of 6 MnI and 8 MnII atoms; see Fig. 2(c). The distances between the 6 MnI and MnII atoms were mentioned above and the distances between the surrounding 8 MnII atoms and the central MnII atom fall into three categories, 0.41899a, 0.42317a, and 0.51793a.

O'Keefe and Anderson [17] fascinatingly described the crystal structure of β-Mn as a body-centered cubic "rod packing" structure in which the rods are infinite and made of strings of atoms that can metaphorically be considered as rods. In their view, a rod consists of two MnI-3MnII tetrahedra and a metaprism of 6 MnII atoms being sandwiched between the two tetrahedra. A picture of such unit string is shown in Fig. 2(d), lower panel. These rods can be equivalently envisaged as a sequence of two metaprisms connecting back-to-back with each other. One metaprism is built by 6 MnII and 1 MnI in the center and the other one is the previously mentioned metaprism of 6 MnII (see Fig. 2(d), upper panel). These rods form a compact body-centered cubic structure that is schematically shown in Fig. 2(e). O'Keefe and Anderson [17] figured out the ideal crystal structure for β-Mn based on purely geometrical considerations. They argued that if the side of an equilateral face of the 6 MnII metaprism becomes equal to its other edges, which are also the edges of another crossing metaprism, then we will have as many equal MnII-MnII distances as possible in the structure. This ideal structure corresponds to a symmetry parameter $y = \frac{9-\sqrt{33}}{16} = 0.20346$. An interesting observation is that the y value reported by Shoemaker *et al.* [21] is 0.2022 and the one reported by Preston [22] is 0.206. The former predicts a shorter side for MnII metaprism and the latter a shorter side for the metaprism. It seems rational to believe that the *ideal* y value must be the one anticipated by O'Keefe and Anderson. Assuming the ideal y value for the structure, the number of different NN distances around an MnII relative to the surrounding 8 MnII reduces from 3 to 2. For the internal parameter x, assuming the six short distances between MnI-MnII to be equal, we get $x = \frac{1}{9+\sqrt{33}} = 0.0678$. This value is comparable to the values reported by Shoemaker *et al.* [21] (0.0636) and by Preston [22] or Kasper and Roberts [2] (0.061). In our study, we have adopted the internal structural parameters from Shoemaker *et al.* [21]. Therefore, all of the distances mentioned above correspond to their set of x and y values.

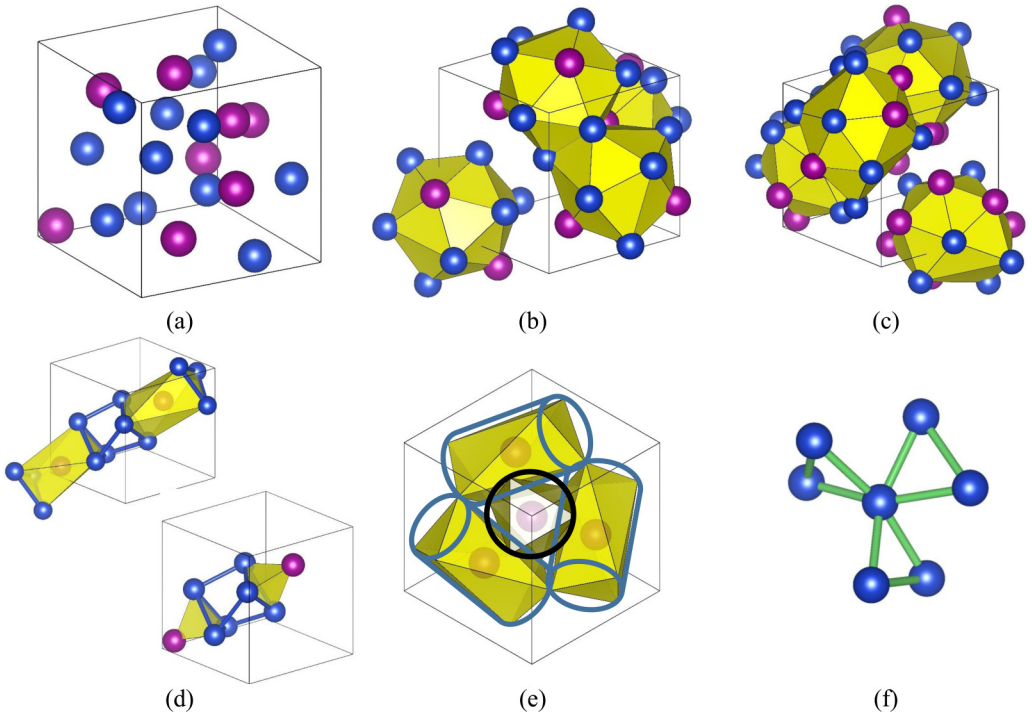

FIG. 2. Analysis of crystal structure of β-Mn. (a) Crystal structure of β-Mn, MnI is denoted by purple and MnII by dark blue. Coordination polyhedra around (b) MnI and (c) MnII. (d) Units of atomic strings in rod packing scheme composed of a metaprism and a tetrahedron lower figure and two metaprism upper figure. (e) Rod packing scheme of O'Keefe and Anderson [17] represented using the metaprism introduced in (d). (f) Three-dimensional corner-sharing triangular network made of MnII atoms.

The magnetic structure of β-Mn is closely related to its peculiar crystal structure. Experimentally it is known that at high temperatures β-Mn is paramagnetic [19,23] and, surprisingly, it remains paramagnetic down to temperatures as low as 1.4 K [24], where the β phase can be obtained by quenching. A large electronic specific heat and the existence of a sizable moment on MnII site are indicative of strong magnetic fluctuations at very low temperatures which may be related to a "quantum spin liquid" state. The effect of geometrical frustration on magnetic properties of low-dimensional lattices such as the Kagomé lattice has been the subject of comprehensive research. This concept has been extended to three-dimensional lattices like fcc lattice and the corner-sharing tetrahedral lattice [25]. The pyrochlore structure is one example where frustration due to the corner-sharing tetrahedra can be found. A frustrated lattice lacks any form of magnetic order down to very low temperatures. For β-Mn as a three-dimensional structure, there is no corner-sharing tetrahedral structure. However, one can modify the concept of corner-sharing triangles, i.e., Kagomé lattice, to explain the magnetic properties of β-Mn. If we consider only MnII atoms in the lattice, we observe that there is a corner-sharing three-dimensional Kagomé like lattice where the dihehral angle between two adjacent triangles is $\cos^{-1}(1/3)$ [see Fig. 2(f). Canals and Lacroix [26] studied the possibility of magnetic ordering in such a network using a mean field classical Heisenberg model. They showed that such a model predicts no order at any temperature on this lattice.

Kasper and Roberts [2] tried to experimentally analyze the magnetic structure of β-Mn using neutron diffraction at 4.2 K. They observed no coherent magnetic scattering and, therefore, could not assign any magnetic moment to any crystallographic site in the structure. Nakamura *et al.* [24] used nuclear magnetic resonance (NMR) technique and polarized neutron scattering to thoroughly investigate the magnetic structure and thermodynamic properties of β-Mn alloyed with Al as well as of pure β-Mn. Their results indicate that the MnII atoms possess a sizable paramagnetic moment, while the MnI atoms are either nonmagnetic or have very small magnetic moments. They also reported that, upon alloying β-Mn with Al, Al atoms preferentially occupy MnII sites and cause the formation of local moments on MnII. This way, the frustration is released and causes a transformation from the paramagnetic state to a spin-glass state.

ASW calculations of β-Mn by Sliwko *et al.* [10] predicted a nonmagnetic ground state for the experimental volume. For expanded volume by 3%, a ferrimagnetic state was predicted with moments of $0.15\mu_B$ on MnI and $-0.57\mu_B$ on MnII. Asada [9] calculated the magnetic structure of β-Mn using the LMTO method. Three magnetic structures were considered: nonmagnetic, ferrimagnetic, and nearly least-frustrated (NLF) antiferromagnetic. For the NLF setup, the moments on MnI were parallel, but the moments on MnII were forced to form a configuration to make the frustration "least" possible. At the experimental volume, calculations for NLF-AF structure gave almost nonmagnetic MnI and a moment of $\sim 2\mu_B$ on MnII. At the expanded theoretical lattice parameter of 6.366 Å, a moment of $0.2\mu_B$ for MnI and a moment of $2.38\mu_B$ for MnII have been predicted.

Hafner and Hobbs [8] extended their study of α-Mn to other allotropes of Mn, including β-Mn. In their study, first-

TABLE II. Crystallographic and magnetic moment data for β-Mn. All the magnetic moments have been computed at the theoretical equilibrium volume.

	MnI	MnII
Number of atoms	8	12
Coordination number	12	14
Atomic radii ratio	1.00	1.13
Volume ratio	1.00	1.43
NN distance	0.374a	0.408a
Type of NN	MnI	MnI
Magnetic Moment (μ_B)—Calculations		
Ref. [9], LMTO, AFM[a]	0.337	1.435
Ref. [9], LMTO, NLF[b]	0.090	2.423
Ref. [8], PAW, FIM[c]	−0.143	0.410
This work, EMTO, DLM	0.75(0.0)[d]	2.25(2.03)[d]

[a]Antiferromagnetic (AFM) structure.
[b]Nearly least frustration (NLF) magnetic structure, cf. Sec. II B.
[c]Ferrimagnetic (FIM) structure.
[d]Averaged value assuming magnetic moment is allowed (quenched) on site MnI.

principles spin-density calculations have been performed using the PAW and LMTO methods where the crystalline, magnetic, and electronic structure of β-Mn were optimized without any symmetry constraint and allowing for nonmagnetic, collinear, and noncollinear magnetic configurations. They reported that nonmagnetic and ferrimagnetic (with small moments on MnII) states are similar in energy for volumes lower than 11.8 Å^3/atom. At expanded volumes, similar to the findings of Sliwko *et al.*, a ferrimagnetic state with large moments on MnII and small but nonnegligible moments on MnI has been observed. A summary of calculated magnetic moments for the β phase is provided in Table II. Hobbs and Hafner [8] suggested that the observed persistence of the magnetic moment on MnII over a wide range of volumes could imply a high degree of frustration of magnetic interactions, a situation quite similar to the behavior of MnIV in α-Mn. Predicted ferrimagnetic state is in contrast with commonly shared opinion that the antiferromagnetic interactions between MnII atoms are stronger than any possible magnetic interaction between MnI and MnII. Repeated predictions of ferrimagnetic state in different studies are indicative of a strong antiferomagnetic interaction between MnI and MnII, which is not surprising considering the NN distances of MnII (see Table II).

III. METHODOLOGY

The present electronic structure calculations are based on density functional theory [27] and employ the exact muffin tin orbitals (EMTO) formalism [28–30]. The coherent potential approximation (CPA) [31] has been exploited to treat magnetic disorder where the paramagnetic state is modeled using the disordered local (magnetic) moment (DLM) approach [32,33]. The electronic structure of the DLM state is represented by that of a disordered alloy consisting of atomic species with spin-up (↑) and spin-down(↓) orientations of magnetic moments, distributed randomly over the sites of the underlying lattice.

The total energies were calculated using GGA [34,35] within the full charge density (FCD) formalism [30,36]. Self-consistent EMTO-CPA calculations were performed using an orbital momentum cutoff $l_{\max} = 3$ for partial waves. Integration over the Brillouin zone was performed using $7 \times 7 \times 7$ k-point girds generated according to the Monkhorst-Pack scheme [37]. As mentioned in Sec. II, due to the difference in atomic coordination of each site, α-Mn forms a self-intermetallic compound. A similar argument holds for β-Mn. Therefore, the fact that Mn atoms on inequivalent sites have different atomic volume, and consequently different electronic structure, must be fully accounted in the calculations.

It is known that total energy calculations for site-centered electronic structure methods require computing three dimensional integrals over Voronoi polyhedra [38]. In EMTO formalism, a site centered method, a Voronoi tessellation is also required in order to construct the potentials for self-consistent calculations in the spherical cell approximation. After self-consistent calculations, the total energies are computed using FCD technique. In FCD calculations, integrals are evaluated inside Voronoi polyhedron of each atom which is to consider the effect of anisotropy of charge and potential. Furthermore, there is a one-to-one correspondence between atomic volumes determined through Voronoi tessellation (VT) and magnetic moments. Since the magnetic contribution to the free energy is directly proportional to magnetic moments, *correct* temperature dependence of magnetic moments yields more accurate results. In *regular* VT, the volume that corresponds to each atom depends on geometry and can be considered as an output rather than an input parameter. However, there are other tessellation methods that can take into account and control the difference in atomic radii in the crystal.

Laguerre tessellation is one of them and we have implemented in the EMTO code the Laguerre tessellation technique using Voro++ code developed by C. Rycroft [39,40]. To start the calculation, relative atomic radii must be specified for the atoms occupying the different sites. The atomic radii have been calculated by overlapping atomic Hartree potentials and locating the the maximum point on the bond between neighboring atoms, i.e., the point where to atomic Hartree potentials intersect. Having obtained the ratio of these radii, Lauguerre tessellation can be carried out. The relative atomic radii and corresponding atomic volumes obtained as a result are given in Tables I and II.

Thermodynamics of materials in first-principle-based schemes can be described by means of the Helmholtz free energy calculated as a function of volume and temperature (i.e., canonical ensemble). To calculate the Helmholtz free energy, $F = -k_B T \ln(Z)$, the partition function Z must be known for all relevant degrees of freedom, i.e., electronic, magnetic, and vibrational. For a disordered magnetic system at elevated temperature, the phase-space to be considered is intractably huge. Therefore, some approach other than direct sampling must be considered to deal with such a system. One fact that can considerably simplifies the problem is that not all degrees of freedom have the same dynamic. In other words, there are *faster* and *slower* degrees of freedom. Our approach similar to previous studies [13–15] is to separate fast and slow degrees of freedom and treat them adiabatically. This so called coarse-graining of free energies can be done

for the system under study by equilibrating the atoms first with respect to the faster degrees of freedom (electronic and magnetic); see Refs. [41,42] for a comprehensive introduction to coarse-graining of free energy. The so obtained partial free energy is then used as a potential energy to describe lattice vibrations (the slower degrees of freedom). Anharmonic effects beyond the expansion of lattice, which play important role near to melting point [43,44], is not explicitly considered in this study. It is also noteworthy that electronic and magnetic contributions calculated in this work correspond to static lattice approximation, it has been shown that there is a significant influence of considering explicit vibrations in the case of Fe [45,46]. The procedure of calculating each contribution to the free energy is explained below.

The electronic free-energy contribution is considered through the introduction of the Fermi-Dirac distribution function in the electronic structure and total energy calculations [47]. The Fermi-Dirac distribution introduces a smearing of the density of states near the Fermi level. In *ab initio* Green's-function-based methods such as EMTO, the Fermi-Dirac distribution is introduced into all the contour integrals over complex energy, with additional computations of residues at a number of complex energy points corresponding to Matsubara frequencies (poles of the Fermi function) [48]. The electronic entropy, $S_{\rm el}$ is evaluated using an additional contour integral,

$$S_{\rm el} = k_B \int (n(z)\{f(z)\ln[f(z)] + [1-f(z)]\ln[1-f(z)]\})dz, \quad (1)$$

where k_B is the Boltzmann constant, $n(z)$ is the electron density of states at complex energy z, and f is the Fermi-Dirac distribution function. The above integral is self-consistently evaluated on a contour which starts from below the bottom of the valence band on the real energy axis and extends to a cutoff energy well above the Fermi level.

The magnetic free-energy contributions are evaluated in this work within the mean-field approximation based on the entropy expression accounting for the transverse spin fluctuations [49] in a paramagnetic lattice gas,

$$S_{\rm mag} = k_B \sum_i N_i \ln(\mu_i + 1). \quad (2)$$

Here μ_i is the magnitude of local magnetic moment an atom at site i in the DLM state treated using EMTO-CPA and N_i is multiplicity (the number of type i positions in the primitive cell). The magnetic moments are calculated self-consistently as to minimize the partial Helmholtz free energy [50],

$$F_{\rm el,mag}(T,V) = E(T,V) - T(S_{\rm mag}(T,V) + S_{\rm el}(T,V)). \quad (3)$$

In the linear response treatment the minimization can be achieved by adding a rigid shift to the one electron potentials for the spin-up $\uparrow$ and spin-down $\downarrow$ electrons (in the local spin coordinate framework on every atom),

$$\Delta U_i^{\uparrow,\downarrow} = \pm \frac{k_B T}{\mu_i + 1}, \quad (4)$$

to enhance or induce the magnetic moment.

Vibrational contribution to the free energy is calculated using Debye-Grüneisen model (DGM) following closely the formalism of Moruzzi, Janak, and Schwarz (MJS) [51]. According to the adiabatic approximation, DGM is the next step based on the obtained partial free energy, Eq. (3). The relation that is used to compute the Debye temperature is

$$\Theta_D = 41.63\left[\frac{r_{ws}B}{M}\right]^{1/2}, \quad (5)$$

where Θ_D is Debye temperature, r_{ws} is Wigner-Seitz radius, B is bulk modulus, and M is the atomic weight. The coefficient 41.63 in above equation follows from the argument proposed in MJS approach that an experimental relation can be used to relate the sound velocity to the bulk modulus in cubic nonmagnetic metals. However, in contrast to MJS's approach, we circumvent the use of Grüneisen parameter. Instead, Eq. (5) is evaluated for each volume. The total Helmholtz free energy of the system can be expressed as the sum of partial free energy contributions,

$$F(V,T) = F_{\rm el,mag}(V,T) + E_D(V,T) - TS_D(V,T). \quad (6)$$

Here E_D and S_D are the energy and entropy expressions in the Debye model. The final expression for the free energy is

$$F(V,T) = F_{\rm el,mag}(V,T) - k_B T[D(\Theta_D/T) - 3\ln(1-e^{-\Theta_D/T})] + \frac{9}{8}k_B\Theta_D, \quad (7)$$

where $D(x)$ is the Debye function and the last term corresponds to zero-point energy.

IV. RESULTS AND DISCUSSION

The DLM picture of paramagnetic state can be considered a good approximation for paramagnetic phase when there is evidence for presence of local moments. Experimental data on magnetic susceptibility may indicate the presence of local moments or spin fluctuations. As mentioned in Sec. II A, Nagasawa and Uchimani measured the magnetic susceptibility of pure α-Mn as well as dilute α-MnV, α-MnCr, α-MnFe, and α-MnCo alloys. An interesting observation in their experiment is that there exists a susceptibility maximum somewhere *above* the Néel temperature. For example, for pure α-Mn the susceptibility maximum occurs at 165 K and varies systematically with alloying. Above the maximum, the susceptibility exhibits a Cure-Weiss behavior. One explanation to this phenomenon was suggested by Misawa [52] who related the anomalous susceptibility maximum to the logarithmic term in Fermi liquid theory. With regards to the evidence for temperature-induced magnetic moments or spin fluctuations in α-Mn, nuclear magnetic resonance (NMR) measurements [53] of Knight shift clearly indicated the existence of local moments on sites I, II, and III. As discussed in Sec. II, there is no consensus about the nature and magnitude of the magnetic moment on site IV. This issue will be addressed in Sec. IV.

Regarding β-Mn phase, there are two sets of experimental data available on high-temperature magnetic susceptibility [23,54]. These datasets disagree with each other on the temperature dependence of susceptibility: Ref. [54] reports a temperature independent behavior, while the data of Ref. [23] suggest a temperature dependent behavior. Sliwko *et al.* [10] stated that in this system because of the shape of density of

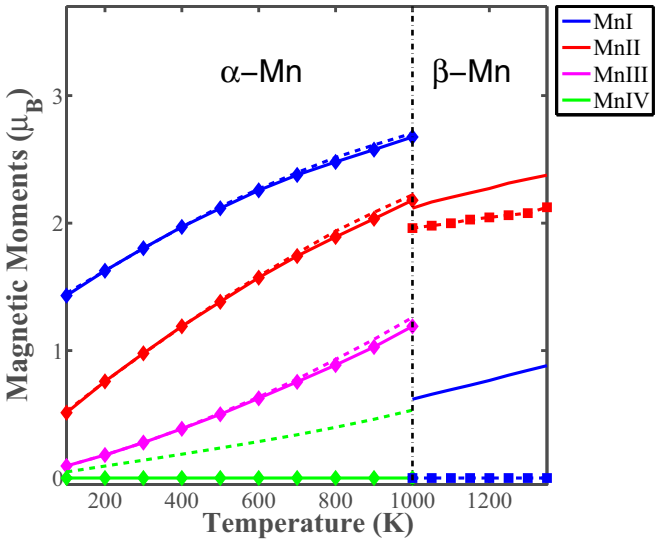

FIG. 3. Variation of magnetic moments as a function of temperature on the four inequivalent sites in α-Mn and the two sites in β-Mn. For α-Mn lines with (without) symbols show the results of calculations when magnetic excitation on MnIV is switched off (on) and for β-Mn when the magnetic excitation on MnI is switched on (off).

states $n(\epsilon)$ and its derivatives at the Fermi level ϵ_f, $n'(\epsilon_f) < 0, n''(\epsilon_f) \rightarrow 0$, the magnetic susceptibility (Pauli paramagnetic contribution) $\chi(T)$ should rise with increasing temperature. At elevated temperatures, Curie-Weiss behavior could be expected if local moments or spin fluctuation are present. So, there could be a competition between the effect mentioned above to increase the susceptibility and the $1/T$ Curie-law-type behavior (local moment or spin fluctuations paramagnetism) to decrease χ. It is therefore logical to conclude that χ could be weakly temperature dependent or even temperature independent depending on which contribution plays a more significant role. It is mentioned above that the experimental results of Nagasawa [19] show a temperature independent trend. In contrast, another set of experimental data [23] confirm the prediction of calculations that there is a slight increase in χ with the increase of temperature. To resolve this disagreement for existence of a local moment, low temperature experimental data could be helpful. Measurements by Nakamura *et al.* [24] give rather sizable moments on site II at temperatures as low as 1.4 K (see Sec. II B for more details). So, it seems reasonable to believe that at elevated temperatures, the magnetic moment on MnII is well developed, i.e., is well localized, and its magnitude is larger than 1.4 K.

Figure 3 shows the variation of magnetic moments for the inequivalent sites in α- and β-Mn with temperature. The general trend for all moments is to grow with temperature. This type of behavior, corresponding to temperature-induced or temperature-enhanced magnetic moments (also referred to as spin fluctuations) has been the subject of extensive research (for a detailed explanation, the reader is referred to the book by Mohn [59]). In the fluctuating spin picture of finite temperature moments, a typical trend is the reduction of magnetic moment due to spin fluctuations below Curie-Néel temperature, and the increase of the averaged paramagnetic moments above the transition temperature. For this reason, it seems plausible to compare the values of the magnetic moments (averaged over the temperature intervals for the two Mn phases in Fig. 3) with the available literature data on low temperature moments. This comparison is made in Tables I and II.

Another point to realize from Fig. 3 is the relationship between the NN distance and the magnitude of magnetic moment for the different crystallographic sites in both α- and β-Mn. To check the debated nature of magnetic moment of MnIV in α-Mn, we *switched off* magnetic excitations in the self-consistent treatment, Eqs. (2)–(4), of magnetic moment on this site as a localized moment and recalculated the electronic structure and properties. (This treatment causes the magnetic moment of MnIV to vanish.) A very interesting fact is that although MnIV constitutes 75% of the coordination shell around MnI, 56% around MnII, and 38% around MnIII (see Table I), switching on or off the magnetic moment on this site does not have a significant effect on the magnitude of magnetic moments of the other sites. This observation can be compared to previous ASW calculations [10] where it was concluded that magnetic moment on site IV *is induced* by the moments on other sites (in Sec. II A we noted that the coordination polyhedron of site IV is an icosahedron made up by 1 MnI, 3 Mn II, 5 Mn III, and 3 MnIV). In contrast, switching off the debatable magnetic moment of MnI atoms in β-Mn, which constitute of about 43% of the coordination polyhedron around a MnII, has a more pronounced effect on the magnetic moment of MnII, as can be seen in Fig. 3. Switching off the paramagnetic moment on MnI causes a shrinking of the lattice constant, Fig. 4(b), which in turn reduces the paramagnetic moment on MnII. As will discussed in the following paragraphs, the treatment of magnetic moment of MnI has a greater effect on the heat capacity and thermal expansion of β-Mn. In Fig. 3 we can see that MnII possesses a rather large magnetic moment and despite this, it remains to be paramagnetic. Model calculations perhaps can shed more light on this question.

The lattice parameter is plotted as a function of temperature in Fig. 4(a) for α-Mn and in Fig. 4(b) for β-Mn. Along with the calculated results, available experimental data for the lattice parameter are plotted. The background of these Figures shows contour plots of Helmholtz free energy as a function of temperature and lattice parameter. Figure 4(a) also shows that switching off the paramagnetic moment on MnIV in α-Mn has a visible effect on the lattice parameter only at very high temperatures. Even at those temperatures, the effect is small. The calculations systematically underestimate the lattice parameter, by about 2.8% at 100 K in comparison with experimental data by Lawson *et al.* [7] and by ~3.14% at 1000 K in comparison with experimental data of Ref. [56]. Since the temperature variation of the lattice parameter turns out to be nonlinear, in Fig. 4(a) we also show a nonlinear fit to the experimental data obtained in the thermodynamic modeling of Mn by Qiu and van der Zwaag [57] (green line). The comparison of our results with the curve confirms that the present calculations systematically underestimate the lattice parameter in the considered temperature range.

Let us now consider the effect of switching on and off the paramagnetic moment of MnI on the thermal expansion of β-Mn. One can see from Fig. 4(b) that the lattice parameter of β-Mn is also systematically underestimated by

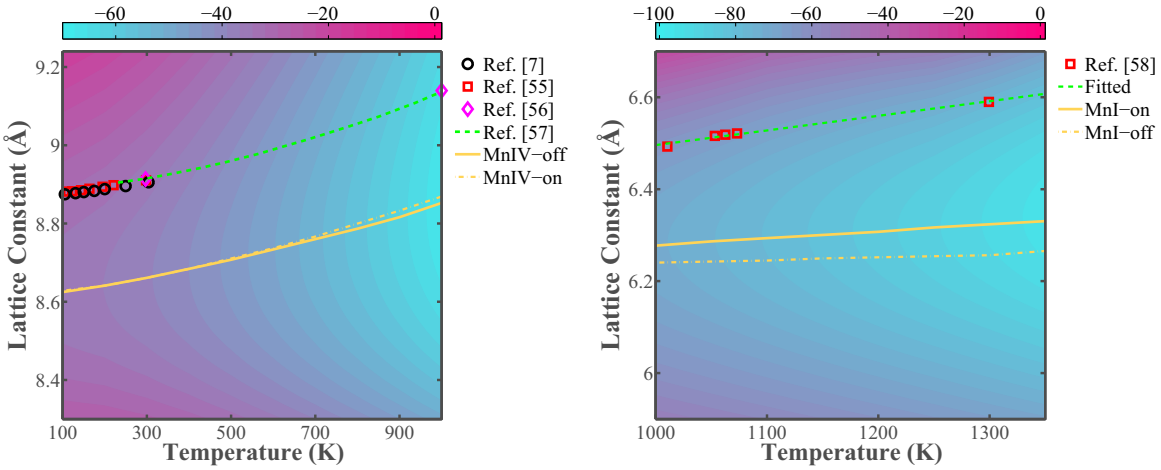

(a) α-Mn (b) β-Mn

FIG. 4. Calculated temperature dependence of the lattice parameter for (a) α-Mn and (b) β-Mn. In both panels the background is a contour plot of the Helmholtz free energy as a function of temperature and lattice parameter. The unit of color legend is mRy. Labels MnIV-off and MnIV-on in (a) correspond to switching off and on the magnetic moment of MnIV. Experimental data are from Refs. [7,55,56]. Thermodynamic modeling data are from Ref. [57]. Labels MnI-on and MnI-off in (b) correspond to switching on and off the magnetic moment of MnI. Experimental data are from Ref. [58].

the present calculations in the considered temperature range. The deviation from experimental data of Ref. [58] is 3.37% at 1000 K and increases to 4.19% at 1350 K. Contrary to the α-Mn case where the deviation is almost constant over the whole considered temperature range, for β-Mn the error increases with the increase of temperature which means that the linear thermal expansion coefficient (TEC) is underestimated. When the paramagnetic moment on site I is switched off, the error in lattice parameter further increases to $\sim$4% at 1000 K and $\sim$5% at 1350 K. The TEC extracted from a linear fit to data of Ref. [58], $a(T) = 6.2777 + 3.1826 \times 10^{-4} T$ (Å), is 48.6×10^{-6} K^{-1} while the present calculations with (without) the magnetic moment on site I yield 24.0×10^{-6} K^{-1} (9.0×10^{-6} K^{-1}). These results imply that the entropy contribution due to the paramagnetic moment of MnI is important for describing the thermal expansion of β-Mn. Consequently, from a thermodynamic consideration, we conclude that there is a possibility for the existence of a paramagnetic moment on site I in β-Mn at elevated temperatures. This is in line with a recent neutron scattering study of β-$Mn_{1-x}Co_x$ alloy by Stewart and Cywinski [60] which gives experimental evidence for the existence of such a moment on site I.

The calculated bulk modulus from the electronic partial free energy of α-Mn at 300 K is 192.9 GPa that is appreciably larger than an experimentally obtained value of 158 GPa (at ambient conditions) reported by Ref. [63]. Hobbs *et al.* [6] reported a calculated value of 188 GPa for the antiferromagnetic structure and about 260 GPa for a nonmagnetic setup. Sliwko *et al.* [10] reported a bulk modulus of 139 GPa for a collinear antiferromagnetic structure at the experimental volume, which shows that there is a considerable scatter even among similar theoretical treatments. For 1000 K, we get a bulk modulus value of 121 GPa which is by 44% lower than the value at 100 K. The rather strong softening effect of temperature on the bulk modulus can be schematically seen in Fig. 4(a) where the curvature of free energy around the equilibrium volume, which is proportional to the bulk modulus, gets shallower as the temperature increases. The softness of elemental Mn is rather well-known, but the cause to this softness is not well understood. Obviously, the magneto-volume effect plays a crucial role in this case, but quantifying this effect from first-principles remains to be a challenge.

The calculated bulk modulus from the electronic partial free energy of β-Mn at 1000 K is as high as 247 GPa, while it is 208 GPa at 1350 K, which is a 15.9% reduction. Similar values of bulk modulus corresponding to 0 K were reported by Hobbs and Hafner [8], 269 GPa for the ferrimagnetic and 300 GPa for the nonmagnetic state. These bulk modulus values are exceptionally high and comparable to those reached in 4*d* or 5*d* metals. A high value of the bulk modulus of β-Mn can be anticipated from Fig. 4(b) where it corresponds to a rather strong curvature of the Helmholtz free energy (and a moderate decrease in the curvature with temperature).

The calculated heat capacity, C_p, and its decomposition to various contributions, is plotted as a function of temperature in Fig. 5(a). We compare our results with the compilation of experiments by Desai [61] where the available experimental data for heat capacity of Mn have been critically assessed and a set of most reliable and consistent data was recommended. With respect to the recommended values by Desai [61], our calculations slightly underestimate the heat capacity of α-Mn below 300 K and overestimate it above that temperature. The maximum difference with Desai's data is at 1000 K where the deviation is about 8.97% (18.50%) for the magnetic moment on site IV treated as switched off (on). The treatment of magnetic moment on site IV did not have a significant effect on the lattice parameter and magnetic moments of Mn atoms occupying the other sites. However, switching on the magnetic moment of MnIV causes a considerable overestimation of C_p. On the basis of thermodynamic consideration, we suggest that site IV could carry a paramagnetic moment. This suggestion is in agreement with experimental data on the Knight shift

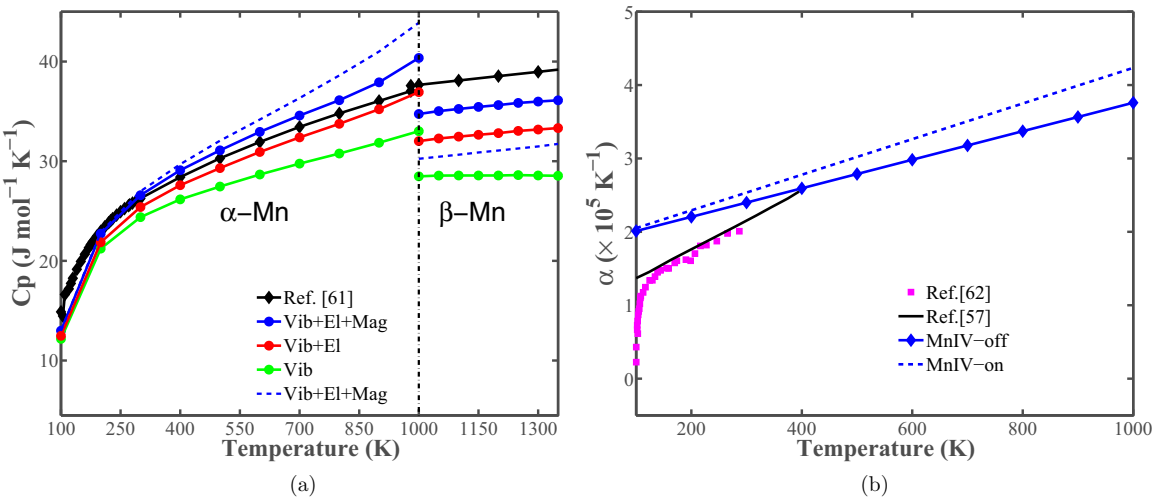

FIG. 5. (a) Heat capacity C_p as a function of temperature for α- and β-Mn. Black solid line with $\diamond$ markers represents critically assessed experimental data compiled by Desai, Ref. [61]. For α-Mn, solid lines with $\circ$ markers correspond to heat capacity contributions evaluated with the magnetic moment of MnIV *switched off* and the dashed line represents the total heat capacity calculated with the magnetic moment on MnIV *switched on*. For β-Mn, the solid lines with $\circ$ markers show the results obtained with the magnetic moment MnI *switched on* and the dashed line represents the total heat capacity calculated with the MnI *switched off*. (b) Linear thermal expansion coefficient of α-Mn as function of temperature. Experimental points are from Ref. [62], the black line is from thermodynamic modeling Ref. [57]. The meaning of labels for the solid and dashed blue lines is the same as in Fig. 4(a) for α-Mn.

for paramagnetic α-Mn by Nagasawa and Murayama [53,64]. They found that the Knight shift is the greatest for sites I and II, while for site III it is small and for site IV the shift is nearly zero. This experimental result is consistent with the trend observed in Figs. 3 and 5(a).

One can see from Fig. 5(a) that the balance of different contributions to C_p of α-Mn is rather temperature dependent. Around 1000 K, where the different contributions should have their greatest magnitude, lattice vibrations contribute 81% while magnetic and electronic excitations together contribute 18% to the C_p. Unlike the case of α-Mn, the calculated C_p of β-Mn is underestimated in comparison to Desai's data in whole temperature range. Excluding the magnetic moment on site I leads to further underestimation of the C_p. Lattice vibrations account for 78% of C_p while the electronic and magnetic excitations contribute the remaining 22%, on average.

The calculated TEC, $\alpha = d\ln(a)/dT$, for α phase is plotted as a function of temperature in Fig. 5(b). To calculate TEC, we fitted the calculated lattice parameter data shown in Fig. 4(a) with a second-order polynomial. We also tried fitting other functions to calculate TEC, the lower and intermediate temperatures appear to be independent of type of fitting function but at high temperatures, the TEC is very sensitive to the choice of fitting function. The reason for choosing the second-order polynomial was that it is the best representation of the calculated data of the lattice parameter. In comparison with the experimental data of Ref. [62], we have overestimated the thermal expansion. For instance at 287 K, the thermal expansion is overestimated by 15%. It is known that below the Néel temperature 97 K, there is a negative TEC and above it, the TEC becomes positive [65]. So, the highly nonlinear behavior of experimental points observed in Fig. 5(b) around 100 K is due to the second-order magnetic phase transition. Unfortunately, the available experimental data are concerned with low/intermediate temperatures and there is a lack of data for TEC of α-Mn at high temperatures. From the available experimental information, it is difficult to speculate about the behavior of TEC at high temperatures. Therefore, from the calculated lattice parameter and its difference to experiment, we can expect that the present form of TEC should not be very different from the experimentally observed one.

At 100 K, lattice vibrations contribute 73.5% to TEC and at 1000 K the lattice contribution increases to 85.2% according to the present calculations. On the other hand, the magnetic and electronic contributions to TEC are substantial: they amount to 26.5% of TEC at 100 K and 14.8% of it at 1000 K. It is expected that lattice vibrations give the main contribution to TEC. Furthermore, the effect of vibrational disorder becomes the dominant one at high temperatures, and this is a reason that any thermodynamic model should include it. Above we discussed the effect of switching on and off the magnetic excitations of MnI on TEC of β-Mn. The vibrational contribution to TEC of β-phase is about 68.6% and is rather independent of temperature. Together electronic and magnetic degrees of freedom contribute 31.4% to the lattice expansion, a more substantial contribution than in the case of α-Mn.

V. CONCLUSION

The thermodynamic properties of α- and β-Mn have been computed using first-principles modeling of free energy. To study paramagnetic state at elevated temperatures, one must solve the computationally expensive problem of treating thermal, magnetic, and electronic disorders simultaneously. Using adiabatic approximation, we derived thermodynamic properties of these phases in the paramagnetic state. In this approximation, faster degrees of freedom, i.e., electronic and magnetic, are equilibrated and thereafter slower degree of

freedom, i.e., vibrational. The modeling approach used in this study is computationally much more efficient than direct sampling methods, and, from the formalism point of view, is more straightforward. To treat electronic disorder, the Fermi-Dirac distribution is introduced in the electronic structure calculations. To treat magnetic disorder, a mean-field expression for the transverse spin fluctuations in a paramagnetic lattice gas has been used. To treat vibrational disorder the Debye-Grüneisen model (DGM) has been employed. We closely follow the Moruzzi, Janak, and Schwarz (MJS) formalism to set up parameters of DGM from partial free energies. In this way, we adiabatically connect different degrees of freedom. Considering the discussion about the nature of paramagnetic moments of site IV of α-Mn and site I of β-Mn, we show, based on thermodynamic arguments, why the former should be zero and the latter nonzero. The present results for the lattice parameter, thermal expansion coefficient, and heat capacity are in good agreement with available experimental data.

ACKNOWLEDGMENTS

The authors are thankful to L. Leach for her valuable comments on the manuscript. Discussions with S. Bigdeli and M. Selleby are acknowledged. This work was performed within the VINNEX center Hero-m financed by the Swedish Governmental Agency for Innovation Systems (VINNOVA), Swedish industry, and the KTH Royal Institute of Techonology. H.E. acknowledges the financial support of Jernkontoret in the framework of Axel Ax:son Johnsons fellowship. P.A.K. gratefully acknowledges financial support of the Ministry of Education and Science of the Russian Federation in the framework of Increase Competitiveness Program of National University of Science and Technology "MISiS" (Grant No. K3-2017-034). Computer resources for this study have been provided by the Swedish National Infrastructure for Computing (SNIC) at the National Supercomputer Centre (NSC), Linköping and PDC Center for High Performance Computing at the KTH Royal Institute of Technology, Stockholm.

[1] C. Shull and M. Wilkinson, Rev. Mod. Phys. **25**, 100 (1953).
[2] J. Kasper and B. Roberts, Phys. Rev. **101**, 537 (1956).
[3] J. A. Oberteuffer, J. A. Marcus, L. H. Schwartz, and G. P. Felcher, Phys. Lett. A **28**, 267 (1968).
[4] N. Kunitomi, Y. Yamada, Y. Nakai, and Y. Fujii, J. Appl. Phys. **40**, 1265 (1969).
[5] L. W. Roth, Phys. Rev. **110**, 1333 (1958).
[6] D. Hobbs, J. Hafner, and D. Spišák, Phys. Rev. B **68**, 014407 (2003).
[7] A. C. Lawson, A. C. Larson, M. C. Aronson, S. Johnson, Z. Fisk, P. C. Canfield, J. D. Thompson, and R. B. V. Dreele, J. Appl. Phys. **76**, 7049 (1994).
[8] J. Hafner and D. Hobbs, Phys. Rev. B **68**, 014408 (2003).
[9] T. Asada, J. Magn. Magn. Mater. **140**, 47 (1995).
[10] V. Sliwko, P. Mohn, and K. Schwarz, J. Phys.: Condens. Matter. **6**, 6557 (1994).
[11] M. J. Mehl and D. A. Papaconstantopoulos, Europhys. Lett. **31**, 537 (1995).
[12] F. Süss and U. Krey, J. Magn. Magn. Mater. **125**, 351 (1993).
[13] D. Ma, B. Grabowski, F. Körmann, J. Neugebauer, and D. Raabe, Acta Mater. **100**, 90 (2015).
[14] Z. Li, F. Körmann, B. Grabowski, J. Neugebauer, and D. Raabe, Acta Mater. **136**, 262 (2017).
[15] H. Sawada, K. Kawakami, F. Körmann, B. Grabowski, T. Hickel, and J. Neugebauer, Acta Mater. **102**, 241 (2016).
[16] A. J. Bradley and J. Thewlis, Proc. R. Soc. A **115**, 456 (1927).
[17] M. O'Keefe and S. Andersson, Acta Crystallogr. Sect. A **33**, 914 (1977).
[18] F. R. McFeely, S. Kowalczyk, L. Ley, and D. A. Shirely, Solid State Commun. **15**, 1051 (1974).
[19] H. Nagasawa and M. Uchinami, Phys. Lett. A **42**, 463 (1973).
[20] T. Yamada, J. Phys. Soc. Jpn. **28**, 596 (1970).
[21] C. B. Shoemaker, D. P. Shoemaker, T. E. Hopkins, and S. Yindepit, Acta Crystallogr. Sect. B **34**, 3573 (1978).
[22] G. Preston, Philos. Mag. **5**, 1207 (1928).
[23] R. Kohlhaas and W. Weiss, Z. Naturforsch. A **24**, 287 (2014).
[24] H. Nakamura, K. Yoshimoto, M. Shiga, M. Nishi, and K. Kakurai, J. Phys.: Condens. Matter. **9**, 4701 (1997).
[25] P. W. Anderson, Phys. Rev. **102**, 1008 (1956).
[26] B. Canals and C. Lacroix, Phys. Rev. B **61**, 11251 (2000).
[27] P. Hohenberg and W. Kohn, Phys. Rev. **136**, B864 (1967).
[28] L. Vitos, H. L. Skriver, B. Johansson, and J. Kollar, Comput. Mater. Sci. **18**, 24 (2000).
[29] L. Vitos, Phys. Rev. B **64**, 014107 (2001).
[30] L. Vitos, I. A. Abrikosov, and B. Johansson, Phys. Rev. Lett. **87**, 156401 (2001).
[31] B. L. Gyorffy, Phys. Rev. B **5**, 2382 (1972).
[32] J. Staunton, B. Gyorffy, A. Pindor, G. Stocks, and H. Winter, J. Magn. Magn. Mater. **45**, 15 (1984).
[33] J. Staunton, B. L. Gyorffy, A. J. Pindor, G. M. Stocks, and H. Winter, J. Phys. F **15**, 1387 (1985).
[34] Y. Wang and J. P. Perdew, Phys. Rev. B **44**, 13298 (1991).
[35] J. P. Perdew, J. A. Chevary, S. H. Vosko, K. A. Jackson, M. R. Pederson, D. J. Singh, and C. Fiolhais, Phys. Rev. B **46**, 6671 (1992).
[36] L. Vitos, *Computational Quantum Mechanics for Materials Engineers* (Springer, London, 2007).
[37] H. J. Monkhorst and J. D. Pack, Phys. Rev. B **13**, 5188 (1972).
[38] A. Alam, S. N. Khan, B. G. Wilson, and D. D. Johnson, Phys. Rev. B **84**, 045105 (2011).
[39] C. H. Rycroft, Chaos **19**, 041111 (2009).
[40] C. H. Rycroft, G. S. Grest, J. W. Landry, and M. Z. Bazant, Phys. Rev. E **74**, 021306 (2006).
[41] A. V. Ruban and I. A. Abrikosov, Rep. Prog. Phys. **71**, 046501 (2008).
[42] A. van de Walle and G. Ceder, Rev. Mod. Phys. **74**, 11 (2002).
[43] F. Körmann, B. Grabowski, P. Söderlind, M. Palumbo, S. G. Fries, T. Hickel, and J. Neugebauer, J. Phys.: Condens. Matter **25**, 425401 (2013).
[44] A. I. Duff, T. Davey, D. Korbmacher, A. Glensk, B. Grabowski, J. Neugebauer, and M. M. W. Finnis, Phys. Rev. B **91**, 214311 (2015).

[45] B. Alling, F. Körmann, B. Grabowski, A. Glensk, I. A. Abrikosov, and J. Neugebauer, Phys. Rev. B **93**, 224411 (2016).
[46] X. Zhang, B. Grabowski, F. Körmann, C. Freysoldt, and J. Neugebauer, Phys. Rev. B **95**, 165126 (2017).
[47] N. D. Mermin, Phys. Rev. **137**, A1441 (1965).
[48] K. Wildberger, P. Lang, R. Zeller, and P. H. Dederichs, Phys. Rev. B **52**, 11502 (1995).
[49] A. V. Ruban and M. Dehghani, Phys. Rev. B **94**, 104111 (2016).
[50] L. Vitos, P. A. Korzhavyi, and B. Johansson, Phys. Rev. Lett. **96**, 117210 (2006).
[51] V. L. Moruzzi, J. F. Janak, and K. Schwarz, Phys. Rev. B **37**, 790 (1988).
[52] S. Misawa, Phys. Lett. A **44**, 333 (1973).
[53] S. Murayama and H. Nagasawa, J. Phys. Soc. Jpn. **50**, 1189 (1981).
[54] Y. Nakagawa, J. Phys. Soc. Jpn. **11**, 855 (1956).
[55] J. Marples, Phys. Lett. A **24**, 207 (1967).
[56] G. Johanssen and H. Nitka, Phys. Z. **39**, 440 (1938).
[57] C. Qiu and S. van der Zwaag, J. Phys. Chem. Solids **59**, 167 (1998).
[58] Z. S. Basinski and J. W. Christian, Proc. R. Soc. London, Ser. A **223**, 554 (1954).
[59] P. Mohn, *Magnetism in the Solid State* (Springer, London, 2003).
[60] J. R. Stewart and R. Cywinski, J. Phys.: Condens. Matter. **21**, 124216 (2009).
[61] P. Desai, J. Phys. Chem. Ref. Data **16**, 91 (1987).
[62] N. S. Petrenko, V. P. Popov, and V. A. Finkel, Phys. Lett. A **47**, 471 (1974).
[63] H. Fujihisa and K. Takemura, Phys. Rev. B **52**, 13257 (1995).
[64] H. Nagasawa and S. Murayama, J. Magn. Magn. Mater. **15**, 93 (1980).
[65] B. D. White, R. K. Bollinger, and J. J. Neumeier, Phys. Status Solidi B **252**, 198 (2015).